



The SDSS-HET Survey of *Kepler* Eclipsing Binaries. Description of the Survey and First Results

Suvrath Mahadevan^{1,2}, Chad F. Bender³, Kelly Hambleton⁴, Scott W. Fleming⁵, Rohit Deshpande^{1,2}, Kyle Conroy⁴, Gal Matijević⁴, Leslie Hebb⁶, Arpita Roy⁷, Hasan Ak⁸, Blaž Leban^{4,9}, and Andrej Prša⁴

¹ Department of Astronomy & Astrophysics, The Pennsylvania State University, 525 Davey Lab, University Park, PA 16802, USA; suvrath@astro.psu.edu

² Center for Exoplanets & Habitable Worlds, The Pennsylvania State University, 525 Davey Lab, University Park, PA 16802, USA

³ Department of Astronomy and Steward Observatory, University of Arizona, Tucson, AZ 85721, USA

⁴ Department of Astronomy & Astrophysics, Villanova University, 800 East Lancaster Ave., Villanova, PA 18085, USA; aprsa@villanova.edu

⁵ Space Telescope Science Institute, 3700 San Martin Dr, Baltimore, MD 21218, USA

⁶ Physics Department, Hobart and William Smith Colleges, 300 Pulteney Street, Geneva, NY 14456, USA

⁷ California Institute of Technology, 1200 E California Blvd, Pasadena, CA 91125, USA

⁸ Erciyes University, Science Faculty, Astronomy and Space Sci. Dept., 38039 Kayseri, Turkey

⁹ University of Ljubljana, Dept. of Physics, Jadranska 19, SI-1000 Ljubljana, Slovenia

Received 2018 November 9; revised 2019 July 30; accepted 2019 July 30; published 2019 October 17

Abstract

The *Kepler* mission has provided a treasure trove of eclipsing binaries (EBs), observed at extremely high photometric precision, nearly continuously for several years. We are carrying out a survey of ~ 100 of these EBs to derive dynamical masses and radii with precisions of 3% or better. We use multiplexed near-infrared *H*-band spectroscopy from the Sloan Digital Sky Survey-III and -IV APOGEE instrument and optical spectroscopy from the Hobby–Eberly Telescope High-resolution Spectrograph to derive double-lined spectroscopic orbits and dynamical mass ratios (q) for the EB sample, two of which we showcase in this paper. This orbital information is combined with *Kepler* photometry to derive orbital inclination, dynamical masses of the system components, radii, and temperatures. These measurements are directly applicable for benchmarking stellar models that are integrating the next generation of improvements, such as the magnetic suppression of convection efficiency, updated opacity tables, and fine-tuned equations of state. We selected our EB sample to include systems with low-mass ($M \lesssim 0.8 M_{\odot}$) primary or secondary components, as well as many EBs expected to populate the relatively sparse parameter space below $\sim 0.5 M_{\odot}$. In this paper, we describe our EB sample and the analytical techniques we are utilizing, and also present masses and radii for two systems that inhabit particularly underpopulated regions of mass–radius–period space: KIC 2445134 and KIC 3003991. Our joint spectroscopic and photometric analysis of KIC 2445134 ($q = 0.411 \pm 0.001$) yields masses and radii of $M_A = 1.29 \pm 0.03 M_{\odot}$, $M_B = 0.53 \pm 0.01 M_{\odot}$, $R_A = 1.42 \pm 0.01 R_{\odot}$, $R_B = 0.510 \pm 0.004 R_{\odot}$, and a temperature ratio of $T_B/T_A = 0.635 \pm 0.001$; our analysis of KIC 3003991 ($q = 0.298 \pm 0.006$) yields $M_A = 0.74 \pm 0.04 M_{\odot}$, $M_B = 0.222 \pm 0.007 M_{\odot}$, $R_A = 0.84 \pm 0.01 R_{\odot}$, $R_B = 0.250 \pm 0.004 R_{\odot}$, and a temperature ratio of $T_B/T_A = 0.662 \pm 0.001$.

Key words: binaries: eclipsing – stars: fundamental parameters – stars: low-mass – techniques: photometric – techniques: radial velocities – techniques: spectroscopic

1. Introduction

Eclipsing binaries (EBs) have served as benchmarks for stellar astrophysics for hundreds of years (e.g., Goodricke 1783). Advances in the precision of radial velocity (RV) measurements over the past several decades have steadily improved the precision of masses derived from EBs. Compilations of EBs show that the total number, diversity, and measurement precisions of detached, main-sequence EBs have steadily increased: 72 stars with masses and radii (M , R) measured to $<15\%$ in Popper (1980), 88 stars with M , $R < 2\%$ in Andersen (1991), 188 stars with M , $R < 3\%$ in Torres et al. (2010), and 198 stars with M , $R < 2\%$ in DEBCat,¹⁰ an updated version of Andersen (1991).

Despite this steady growth in sample size, low-mass stars (defined here as $M < 0.8 M_{\odot}$) remain a relatively small fraction of the overall sample. For example, DEBCat contains only 54 stars with $M < 0.8 M_{\odot}$, while the sample of Torres et al. (2010) has only 10 such stars, none of which has an orbital period longer than five days. More recent results are starting to expand

the low-mass sample (e.g., Schwamb et al. 2013; Gómez Maqueo Chew et al. 2014; Zhou et al. 2015; Dittmann et al. 2017; Lubin et al. 2017; Casewell et al. 2018), but a significant increase in sample size is still lacking, predominantly due to the resource expense associated with obtaining high-precision RVs (the method used to derive most of the EB dynamical masses in the current compilations), and because the poor flux ratio of a low-mass K/M dwarf orbiting a larger primary makes it difficult to detect in the optical.

Observations in the near-infrared (NIR) result in the tangible benefit of improving the flux contrast for EBs with a small mass ratio ($q = M_B/M_A$). For example, the flux ratio of an M5 dwarf, with $T_{\text{eff}} \sim 3300$ K, to a G2 dwarf, with $T_{\text{eff}} \sim 5800$ K, is ~ 10 times more favorable in the *H* band than in the *V* band. This allows for the extraction of measured RVs from fainter secondary stars, and therefore extends the lower limit on q for which masses of dwarf stars can be derived. While optical spectra tend to lose sensitivity at $q \sim 0.5$, NIR spectra can push down to $q \sim 0.1$ (Prato et al. 2002; Mazeh et al. 2003; Bender & Simon 2008).

Measurements of selected bright binaries have achieved precisions in mass ratio (in $M \sin i$) of 0.02%–0.42% (Konacki

¹⁰ <http://www.astro.keele.ac.uk/jkt/debcats/>

et al. 2010), but precisions of 1%–3% are still sufficient to distinguish between model parameters (Morales et al. 2010). The high photometric precision of *Kepler* makes it possible to determine the masses of some EBs purely photometrically (Carter et al. 2011; Faigler et al. 2012) via Doppler boosting and ellipsoidal effects (Faigler & Mazeh 2011). While the technique is promising, Carter et al. (2011) achieved only a 10% mass precision using the *Kepler* photometry alone (i.e., without including any spectroscopic RVs), while Faigler et al. (2012) found that only five of their seven binaries had RV semi-amplitudes in agreement with those predicted from their photometric analysis. In a large follow-up program, Tal-Or et al. (2015) observed 281 targets, confirming 70 binary systems while finding that many of their false positives were due to pulsating red giants. The use of spectroscopic RVs therefore remains an essential and reliable method for obtaining mass precisions at the 1%–3% level, motivating the continual use of spectra to measure the stellar masses of EBs.

Stellar models rely on the precision measurements that EBs afford for calibrating the physical parameters used in their calculations (leading to well characterized EBs often being referred to as stellar “benchmarks”). Stars with $M > 0.8 M_{\odot}$ generally agree with theoretical models to within observational uncertainties. Lower-mass stars, however, are often observed to have radii that are 5%–15% larger than model predictions (López-Morales 2007; Morales et al. 2008; Torres et al. 2010; Kraus et al. 2011; Higl & Weiss 2017; Cruz et al. 2018; Kesseli et al. 2018). There is observational and theoretical evidence to suggest that magnetic fields could be the cause (Chabrier et al. 2007; Morales et al. 2010; Feiden & Chaboyer 2013; MacDonald & Mullan 2017), due to interaction with the partially convective outer atmospheres and/or generation of cool starspots at polar latitudes. Unidentified opacity sources have also been suggested (Berger et al. 2006), although a lack of metallicity measurements for many stars in the current EB sample has prevented an in-depth examination of that possible correlation. Models that use a different equation of state than previous works agree with observations of one low-mass *Kepler* EB (KOI-126; Feiden et al. 2011), opening another regime of parameter space to explore.

In this paper we introduce the *SDSS-HET Survey of Kepler EBs*, which is combining *Kepler* photometry with ground-based spectroscopy to precisely measure orbital parameters, dynamical masses and radii, and temperature ratios for a sample of 109 EB candidates selected from the catalog of Kirk et al. (2016) and listed in Table 1. We utilize both optical and NIR spectroscopy to solve these EBs as double-lined spectroscopic binaries (SB2s), and combine these results with *Kepler* photometry to derive masses and radii with precisions of better than 3% for most of the sample, and as good as 1% for a subset. Here we present two objects in our sample. Our complete sample is restricted to EBs that are classified as fully detached and have $H < 13$. Orbital periods range from a few days to more than 100 days. The total sample size is comparable in number to the $M < 2M_{\odot}$ members in Torres et al. (2010) and DEBCat (110 and 285 EBs, respectively), but we have included many EBs with low-mass primary or secondary components in order to substantially increase the population of well measured low-mass stars. One of the reasons why the compilation from Torres et al. (2010) is so useful to the astronomical community is that their study homogeneously recomputed orbital and stellar parameters from the compiled list of literature EBs. Our

survey will intrinsically possess this quality, because our analysis applies a singular set of tools to a homogeneous data set.

In Section 2 we describe the facilities and data products we are using, and in Section 3 we discuss the analytical techniques applied to the spectroscopy and photometry, as well as probabilistic analysis that we use to derive realistic parameter uncertainties. In Section 4 we present two low-mass EBs from our sample, and provide our derived orbits, masses, and radii for these systems. In Section 5 we discuss these systems in the context of the pre-existing population of precisely measured low-mass EBs, and describe our plans for analyzing the remainder of our *Kepler* EB sample. As part of this program, we constructed a semi-automated reduction pipeline for the HET High-resolution Spectrograph, which we describe in the Appendix.

2. Facilities and Data Sets

2.1. The Kepler Mission

Kepler is a space-borne, 0.95 m, high-precision photometer equipped with a broadband filter covering 420–865 nm. From 2009 to 2013, *Kepler* monitored a single field located 13°5′ above the Galactic plane in the direction of Cygnus, with a mission to detect transiting, habitable-zone exoplanets (Borucki et al. 2010). Its ability to conduct photometry with high precision (~ 80 ppm for $K_p = 12$; Caldwell et al. 2010) and to observe with a nearly continuous cadence facilitated numerous ancillary stellar astrophysics programs, including the detection of EBs over a range of orbital periods that are challenging to observe from the ground. The majority of *Kepler* EBs are faint (only $\sim 12\%$ of detached systems have $K_p < 12$ in Kirk et al. 2016), and follow-up spectroscopy of such systems requires a combination of large telescopes and long exposure times. The *Kepler EB Catalog*¹¹ (Prša et al. 2011; Slawson et al. 2011; Matijević et al. 2012; Conroy et al. 2014; Abdul-Masih et al. 2016; Kirk et al. 2016) has used *Kepler* photometry to identify thousands of EBs, and has derived extremely precise orbital periods, which greatly simplifies the process of turning individual spectroscopic measurements into an SB2 orbit.

2.2. The SDSS-III APOGEE Spectrometer

The Apache Point Observatory Galactic Evolution Experiment (APOGEE, Majewski et al. 2017) is a fiber-fed, multi-object, near-infrared spectrometer that uses a volume phase holographic grating and a linear array of three Hawaii-2RG detectors to record spectra from 1.51 to 1.68 μm with a spectral resolution of $\lambda/\Delta\lambda \sim 22,500$ (Wilson et al. 2010). The instrument is located at Apache Point Observatory on the 2.5 m telescope of the Sloan Digital Sky Survey (SDSS) (York et al. 2000; Gunn et al. 2006), and was commissioned in the spring and summer of 2011 for a three-year survey aimed at a Galactic evolution experiment (Allende Prieto et al. 2008; Eisenstein et al. 2011). A small fraction of the survey time ($\sim 5\%$) was devoted to ancillary science programs (Zasowski et al. 2013), which include the *Kepler* EB program described in this paper. The spectrograph is stabilized in a vacuum-sealed cryostat cooled via liquid nitrogen, which minimizes thermal variations and yields a typical RV precision of 100–200 m s^{-1} on our EB sample. APOGEE can simultaneously observe 300

¹¹ <http://keplerebs.villanova.edu/>

Table 1
Project EBs Observed

KIC ID	K_p	g	H	P_{cat}	N_{APG}	N_{HET}	Notes
01571511	13.424	13.855	12.041	14.022451	3	9	
02010607	11.347	11.630	10.204	18.632296	3	6	
02162994	14.162	14.696	12.570	4.101595	3	6	
02305372	13.821	14.341	12.201	1.404691	3	0	
02305543	12.545	12.971	11.138	1.362274	3	0	
02306740	13.545	14.025	12.022	10.306987	3	7	
02308957	14.520	15.031	12.916	2.219684	3	6	
02309587	13.925	14.434	12.359	1.838511	3	0	
02309719	12.899	13.335	11.528	54.356360	3	9	
02445134	13.551	13.948	12.201	8.412009	3	8	
02445975	13.513	14.404	12.830	6.777765	3	0	
02447893	14.490	15.134	12.628	0.661620	3	0	
02576692	12.744	13.191	11.371	87.878533	3	8	
02583777	12.735	13.166	11.311	0.958117	3	0	
02708156	10.672	10.672	10.525	1.891272	3	0	
02711114	12.335	12.634	11.115	2.858880	3	0	
02720354	13.116	13.387	11.965	2.821328	3	9	
02860594	13.370	13.613	12.237	5.499945	3	10	
02860788	14.043	14.614	12.255	5.259742	3	0	
02997455	13.800	14.694	11.500	1.129850	3	0	EB Cat FP, No RV Var
03003991	13.926	14.482	12.278	7.244779	6	8	
03120320	10.885	11.280	9.611	10.265613	3	6	
03127817	12.155	12.242	10.590	4.327139	6	9	
03128793	14.633	15.546	12.310	24.679381	6	0	
03130300	14.313	14.696	12.970	11.531282	6	0	EB Cat FP, No RV Var
03230578	13.406	13.860	12.189	6.337611	3	0	
03230787	12.553	12.990	11.141	17.734052	3	8	
03241619	12.524	13.063	10.798	1.703344	3	0	
03247294	13.924	14.353	12.442	67.418828	6	7	
03248033	12.161	12.427	11.019	2.668220	6	0	EB Cat FP, No RV Var
03248332	13.102	13.369	12.012	7.363607	6	6	
03335816	12.084	12.399	10.842	7.422006	3	7	
03339538	13.391	14.106	11.429	14.658014	3	5	
03351945	14.734	15.549	12.605	1.080538	6	0	
03352751	13.444	13.541	12.304	3.495455	6	9	
03439031	11.287	11.503	10.117	5.952026	3	6	
03440230	13.636	13.706	12.486	2.881101	3	0	
03441784	9.729	9.898	9.124	52.568726	3	0	
03443790	11.840	12.164	10.602	1.665784	3	0	EB Cat FP, No RV Var
03449540	14.194	14.533	12.941	3.212006	3	6	
03458919	13.815	14.370	11.512	0.892061	6	0	
03541800	14.367	14.764	12.994	4.662364	3	6	EB Cat FP, No RV Var
03542573	12.161	12.613	10.739	6.942796	3	9	
03556742	14.221	14.957	12.278	0.823013	6	0	EB Cat FP, No RV Var
03558981	13.109	13.715	11.974	2.987858	6	6	
03655326	14.213	14.614	12.980	15.066503	6	0	
03656322	13.061	13.723	11.150	3.663648	6	8	
03656700	12.997	13.553	11.398	0.738528	6	0	EB Cat FP, No RV Var
03749508	13.151	13.536	11.862	1.065734	3	0	
03765771	14.216	14.601	12.897	5.567717	6	0	
03766353	13.968	14.262	12.744	2.666966	6	0	
03846515	12.807	13.148	11.640	1.776084	3	0	
03848919	13.901	14.477	12.141	1.047260	3	0	
03848972	14.489	15.037	12.795	0.741057	3	0	
03849155	13.831	14.393	12.271	1.168313	3	0	
03851193	13.682	14.050	12.478	1.341079	3	7	
03858804	13.778	14.501	11.852	25.951944	6	9	EB Cat FP, No RV Var
03858949	14.576	15.190	12.872	25.951139	6	0	EB Cat FP, No RV Var
03861595	11.432	11.755	10.266	3.849367	6	6	
03867593	13.559	13.735	12.490	73.332022	6	0	
03869825	13.320	13.597	12.180	4.800655	6	8	
03955867	13.547	14.449	11.303	33.659962	3	8	
03957477	12.477	13.001	10.987	0.979052	3	0	
03964562	12.403	12.419	11.903	3.012476	6	0	

Table 1
(Continued)

KIC ID	K_p	g	H	P_{cat}	N_{APG}	N_{HET}	Notes
03965242	14.060	14.681	12.291	0.996722	6	0	
03970233	14.034	14.656	12.333	8.254914	6	7	
03971315	13.664	14.039	12.320	9.892277	6	11	EB Cat FP, No RV Var
03973549	14.293	14.801	12.926	1.389955	6	0	
04069063	13.318	13.733	11.932	0.504296	6	0	
04069213	12.739	13.119	11.262	5.194256	6	6	
04075064	14.951	15.712	12.904	61.422806	6	0	
04076952	13.773	14.195	12.438	9.761169	3	8	
04077442	13.512	14.348	11.368	0.692843	6	0	
04078693	13.485	14.131	11.794	2.756531	6	0	
04157488	13.961	14.379	12.467	5.197420	3	6	
04165960	13.889	14.196	12.664	13.549178	6	0	
04178389	14.228	14.695	12.708	23.210523	6	10	
04275328	13.303	13.607	11.976	6.150530	6	6	EB Cat FP, No RV Var
04281895	12.256	12.758	10.650	9.543588	6	8	
04285087	12.785	13.188	11.397	4.486031	6	8	
04372379	13.810	14.091	12.689	4.535183	6	7	
04376644	13.767	14.193	12.371	27.677704	6	6	
04473933	12.030	12.868	9.237	103.592625	6	8	
04477830	13.548	13.894	12.336	3.384909	6	6	EB Cat FP, No RV Var
04484356	14.235	14.872	12.359	1.144160	6	0	
04570555	11.540	12.312	9.483	4.750303	6	7	EB Cat FP, No RV Var
04570949	13.308	13.644	12.134	1.544929	6	0	
04660997	12.317	12.778	10.763	0.562561	6	0	
04665989	13.016	13.215	12.000	2.248067	6	0	
04671584	13.742	14.137	12.346	5.593325	6	6	
04672010	14.602	15.530	12.445	0.963042	6	0	
04753561	14.928	15.918	12.647	4.944922	6	0	EB Cat FP, No RV Var
04758368	10.805	11.670	8.516	3.749954	6	12	
04840327	12.688	13.077	11.256	26.737133	6	8	
04847832	12.450	13.202	11.051	30.960237	6	6	
04850874	12.228	12.379	11.037	1.775906	6	0	
04851217	11.108	11.316	10.282	2.470280	6	0	
04931073	11.957	12.179	10.842	26.951236	6	9	
04932691	13.627	13.815	12.641	18.112079	6	0	
05017058	13.140	13.559	11.833	2.323895	6	0	
05025294	13.266	13.704	11.795	5.462690	6	7	
05193386	13.998	14.703	12.054	21.378294	6	8	
05199426	14.080	14.558	12.532	78.604362	6	6	
05284133	12.444	12.501	11.773	8.784576	6	5	
05285607	11.419	11.684	10.304	3.899401	6	7	
05288543	13.585	13.584	12.113	3.457076	6	7	
05376836	14.041	14.516	12.571	3.479425	6	0	
05460835	14.293	14.720	12.855	21.539274	6	0	
05462901	15.953	17.140	13.201	5.270726	6	0	

targets over the telescope’s 3 σ diameter field of view, which is also fortuitously the approximate size of each *Kepler* module. This multiplexing capability allows us to efficiently observe many EBs with a single integration, also referred to as a *visit*. Each *visit* typically comprises eight consecutive eight-minute exposures, which are later combined by the APOGEE data reduction pipeline (Nidever et al. 2015) to produce a single *visit* spectrum with a total integration time of slightly more than one hour. All analysis described in this paper utilizes APOGEE data at the *visit* level of processing.

Our ancillary APOGEE program included two fields overlapping *Kepler* modules centered on the open clusters NGC 6791 (three *visits*) and NGC 6819 (six *visits*). We observed a total of 42 and 67 detached EBs in each field, respectively. All spectra for this program were obtained in 2011, during the first

year of survey operations, and have been publicly released as part of SDSS Data Release 10 (Ahn et al. 2013).

Prior to analyzing the APOGEE spectra, we perform additional post-processing beyond that provided by the APOGEE pipeline. We use a low-order polynomial to remove continuum and normalize each spectrum. Residuals caused by imperfect correction of telluric absorption and sky emission are present in most pipeline-reduced APOGEE spectra; we manually correct these by interpolating over neighboring pixels. The pipeline version used for the DR10 release flagged wavelengths with suspected bad pixels by setting their flux to zero. This flagging complicates our RV measurements because a cross-correlation analysis interprets such pixels as having strong, discrete signal that is not present in correlation templates, which reduces the overall amplitude of a real

correlation signal. We interpolate over these regions to minimize their impact.

2.3. The HET High-resolution Spectrograph

The small number of visits obtained by APOGEE in each of our fields are, by themselves, inadequate for deriving stellar mass at the 3% level for most of our EBs, but the infrared bandwidth provides essential leverage on the low-mass companions in high-contrast systems. Consequently, for 55 of our EBs (Table 1, column 7) we supplemented the APOGEE spectroscopy with optical spectroscopy from the 9.2 m Hobby–Eberly Telescope (hereafter HET) to achieve higher precision in spectroscopic orbital determination for the primary star. The High-resolution Spectrograph (Tull 1998, hereafter HRS) is a visible-light, fiber-fed, cross-dispersed, echelle spectrometer located on the HET (Ramsey et al. 1998). The HET was designed to carry out narrow-field spectroscopy of faint objects, and so is well suited for targets such as our *Kepler* EB sample. The spectrograph is housed in an isolated enclosure in the HET spectrograph room, which provides a moderately stable environment capable of achieving long-term RV stability of 25 m s^{-1} on bright, low-mass, main-sequence stars using standard ThAr emission lamps for wavelength calibration (Bender et al. 2012). The HET operates under a queue-based observing scheme (Shetrone et al. 2007) that allows us to request observations of a target to occur within a narrow time window. This capability allowed us to efficiently observe 55 members of our EB sample from 2011 to 2013, while targeting each system at specific orbital phases. A similar set of observations could not easily be obtained at a classically scheduled facility, making the HET a unique resource for studying binary stars.

We use the HRS with a $2''$ fiber in a configuration that provides a spectral resolution of $\lambda/\Delta\lambda = 30,000$ over a bandwidth from 4076 to 7838 Å, except for a small gap at 5936 Å where light falls between the two HRS CCDs, distributed in 73 spectral orders. This configuration provides a large number of these features, from which we derive precise radial velocities. The HET queue-based observing mode allows for the spectrograph configuration to change multiple times throughout a single night as targeting requests from different observers are carried out. Standard sequences of calibration frames, including biases, flats, and ThAr wavelength references, are typically obtained at the end of the observing session. The echelle and cross-disperser positions are not precisely repeatable at the sub-pixel level, so the standard HET operations introduce a discontinuity between the target and the ThAr observations, which can result in RV shifts of several hundred m s^{-1} . To avoid this, we obtain additional ThAr frames immediately before or after each target observation, without altering the instrument configuration. We do not obtain extra flats because the telescope overhead would be severe and our experience has shown that the misalignment inherent in the standard queue procedures is usually small enough to prevent fringing in reduced images.

To efficiently and uniformly reduce the large HRS data set generated by our *Kepler* EB program, we created a semi-automated data handling pipeline for the HRS. This pipeline is written in the Interactive Data Language (IDL) and carries out image processing, spectral extraction, and wavelength calibration tasks. The Appendix gives a detailed description of the pipeline.

As with the APOGEE spectra, we apply several post-processing steps to our extracted HRS spectra prior to analysis. Each spectral order is continuum-normalized. Strong telluric contamination is mostly restricted to isolated regions at optical wavelengths. Rather than attempt a telluric correction across our HRS bandpass, we choose to retain only those regions of the spectrum with telluric contamination of 0.5% or smaller, modulus a continuity function that preserves large unbroken chunks of spectrum. In practice, we retain eight spectral windows: 4390–5025 Å, 5100–5410 Å, 5475–5680 Å, 5770–5855 Å, 6020–6260 Å, 6365–6430 Å, 6620–6850 Å, and 7450–7580 Å. Finally, sky emission lines are removed by interpolating over neighboring pixels.

3. Analytical Techniques

3.1. Measurement of Radial Velocities

All spectroscopy of unresolved binary stars contain the blended light of both the primary and secondary components. The signal-to-noise ratio (S/N) and the wavelength-dependent contrast ratio of an individual spectrum dictate whether that spectrum can be solved as an SB2 or only as a single-lined spectroscopic binary (SB1). Our APOGEE spectroscopy (Section 2.2) was designed to exploit the NIR contrast advantage of EBs containing a pair of main-sequence stars with a small q , thereby observing the systems as SB2s. Because our target sample contains a wide range of binary types, including EBs with small q , EBs with equal-mass components, and EBs with one or both components evolving or evolved, the suitability of optical or NIR spectroscopy for solving each EB as an SB2 is determined case by case.

We analyze our processed APOGEE and HET spectra identically, using a combination of one-dimensional and two-dimensional cross-correlation algorithms to measure RVs for the primary and secondary components of each EB. For the two-dimensional case, we have implemented the TODCOR algorithm (Zucker & Mazeh 1994) as an interactive IDL program, SXCORR, which allows the user great flexibility in quickly optimizing the correlation templates while examining multiple epochs of spectra. SXCORR simultaneously cross-correlates two template spectra against a target spectrum containing the blended light from a binary to disentangle the component RVs. Our SXCORR implementation of TODCOR includes the maximum-likelihood extension described by Zucker (2003), modified slightly to allow segments of spectrum with variable lengths. SXCORR automatically resamples both target and template spectra into log-lambda wavelength space (Tonry & Davis 1979), as needed depending on the input spectra. Previous investigations have extensively described our procedures for using TODCOR techniques to measure the RVs of an SB2 (e.g., Bender & Simon 2008; Bender et al. 2012; Lockwood et al. 2014), and we refer the interested reader to the descriptions therein. Our one-dimensional correlation analysis is the trivial simplification of the two-dimensional case.

Concurrently with our HRS EB observations, we observed an extensive spectral template library of known single dwarf stars using an identical HRS configuration. This library ranges in spectral type from early F through mid M. Additionally, we have supplemented this library with synthetic templates generated from the PHOENIX-based BT-Settl model grid (Allard et al. 2011). These synthetic models cover a much wider range of T_{eff} , [M/H], and $\log g$ than our observed library, although

some demonstrate substantial discrepancies with observed spectra at high resolution (Terrien et al. 2014) that manifest in our RV analysis as reduced correlation power. To generate a template from the BT-Settl library, we convolve the raw synthetic spectrum to the proper resolution (22,500 for APOGEE, 30,000 for HRS), and resample to three pixels per resolution element. We additionally apply a suite of rotational broadening kernels generated from a four-parameter nonlinear limb-darkening model (Gray 1992; Claret et al. 2012) and the appropriate stellar parameters. We do not have an observed template library for the *H*-band APOGEE spectra, so all APOGEE RVs are measured using BT-Settl templates.

3.2. Binary Star Modeling

To model the *Kepler* light curve with APOGEE and HET RV data simultaneously, we used PHOEBE 1.0 binary star modeling software (Prša & Zwitter 2005), which is based on the Wilson–Devinney code (Wilson & Devinney 1971, hereafter WD). To make certain that there are no numerical or systematic artifacts arising from the choice of the legacy model, we synthesized light and RV curves using PHOEBE 2.1 (Prša et al. 2016) and found no evidence for any discrepancy that exceeds the order of data scatter. We fit the data within a Bayesian framework, by utilizing EMCEE, a PYTHON implementation of the affine invariant Markov chain Monte Carlo (MCMC) ensemble sampler proposed by Goodman & Weare (2010) and implemented by Foreman-Mackey et al. (2013). We model the noise, instrumental variations, and stellar variations caused by spots by employing CELERITE, a Gaussian process (GP) library (Foreman-Mackey et al. 2017). Prior to modeling, we minimally prepared the data by flux-normalizing and stitching the *Kepler* quarters and removing any obvious spurious points. The entire process is streamlined into the pipeline that is capable of processing the data autonomously. We describe the details below.

3.2.1. Uncertainty Determination for the Kepler Data

As the *Kepler* data uncertainties are commonly underestimated, we determined the uncertainties by identifying the standard deviation of sections of the light curve. For each object we identified 10 sections that contained slowly varying instrumental noise and spots, and Gaussian noise. We determined the noise of the 10 sections individually and subsequently used the average as our uncertainty value for all points on the light curve. To ensure we did not underestimate the noise in the light-curve data, we included a Gaussian noise term in our fitting procedure, which is discussed in more detail in Section 3.2.4.

3.2.2. The PHOEBE Model

The PHOEBE modeling software combines the complete treatment of the Roche potential with the detailed treatment of surface and horizon effects such as limb darkening, reflection, and gravity brightening to derive an accurate model of the binary parameters. The current implementation uses the WD method of summing over the discrete trapezoidal surface elements, which cover the distorted stellar surfaces, to determine an accurate representation of the total observed flux, and consequently a complete set of stellar and orbital parameters. PHOEBE incorporates all the functionality of the WD code, but also provides an intuitive graphical user interface

alongside many other improvements, including updated filters, PHOENIX model atmospheres (Husser et al. 2013), and bindings that enable interfacing between PHOEBE and PYTHON.

To decrease the computational cost of using PHOEBE with EMCEE, for each iteration we created the model light curve containing 2000 data points in phase space. We then unfolded this model light curve into time space prior to adding the noise model and determining the log-likelihood. This allowed the light curve to be computed in a relatively short amount of time, but fit the model of the light curve combined with the instrumental and stellar trends to the complete data set.

The light curve and RV data were fit simultaneously. Within our models, we fit the following parameters: inclination, i ; eccentricity, e ; argument of periastron, the angle from the ascending node to periastron, measured in the direction of motion, ω ; the primary and secondary potentials, proportional to the inverse radius, Ω_1 and Ω_2 , respectively; third light l_3 ; gamma velocity, the motion of the center of mass of the binary, γ ; mass ratio, q ; and semimajor axis, sma . We further set the albedos (reflective properties of the stars) and gravity darkening exponents (which relate to the change in temperature of the stars due to their obliquity), to the theoretical values of $A = 0.6$ (Ruciński 1969b) and $\beta = 0.32$ (Lucy 1967) for stars with convective envelopes ($T_{\text{eff}} < 7000$ K) and to $A = 1.0$ (Ruciński 1969a) and $\beta = 1.0$ (von Zeipel 1924) for stars with radiative envelopes ($T_{\text{eff}} > 7000$ K). As Diaz-Cordoves & Gimenez (1992) showed that the square-root limb-darkening model is preferable for objects that radiate toward the IR, we applied the square-root limb-darkening law to our models and updated the limb-darkening coefficients after each iteration. Limb darkening is a thorny issue, with its implications discussed in detail in Prša et al. (2016); it affects eclipse ingress and egress and is degenerate with stellar radii. We use limb-darkening coefficients computed from the PHOENIX model atmospheres for the range of temperatures, surface gravities, and chemical abundances applicable to our systems. We enforced consistency by interpolating the limb-darkening coefficients for any explored combination of atmosphere parameters. While there are inherent limitations to using the square-root limb-darkening model, the compounded systematic effects that arise from its use (compared to other limb-darkening models) are below 0.5%.

3.2.3. MCMC Derived Uncertainties

Objective comparison between masses and radii measured observationally and those predicted by theory requires that realistic uncertainties be derived for the measurements. We use an MCMC sampler to sample the posterior probability distribution function. At each iteration we compute the posterior log-probability distribution function:

$$\log P(\theta|D) = \log P(F|\theta) + \log P(\text{RV}|\theta) + \log P(\theta) + C, \quad (1)$$

where D denotes the data, F are the light-curve measurements, RV are the RV measurements, θ is the parameter vector that contains the fitted parameters (specified in Section 3.2.2), and C is an arbitrary constant. We incorporate EMCEE into our analysis to sample the probability distribution function within a Bayesian framework. A significant advantage of this is that the results are presented as posterior probability distribution

functions, which indicate parameter correlations and provide more robust uncertainty estimates.

MCMC explores the parameter space using a set of walkers, in our case 142. These chains begin with a uniform prior probability distribution for each parameter. At every iteration, each chain assesses its likelihood with respect to that of another chain and then elects whether to move toward that chain. The new parameters are based on the covariance matrix of the two chains. If the move increases the posterior likelihood then it is accepted; if the move decreases it then it may be accepted with a certain probability. During the initial burn-in time, Markov chains are converging toward their maximum-likelihood position. The statistics of a large number of iterations provide converged posterior distributions for the model parameters.

We create a model of all available data (light curves and radial velocities) for each binary star. To assess convergence, we use autocorrelation timescales. The autocorrelation timescale is used to estimate the number of iterations required to generate an independent sample, i.e., the number of iterations required for the chain to “forget” where it started. We require a minimum of 30 autocorrelation timescales to achieve convergence.

Eclipse depths are related to the temperature ratio. To obtain an accurate uncertainty for the temperature ratios, and thus secondary component temperatures, we marginalized over the primary and secondary effective temperatures, and report the posterior probability of the temperature ratio. From this, we calculate the secondary temperature and its uncertainty. The minimal rotational RV that can be derived from APOGEE spectra is limited by the resolving power, allowing us to measure $v_{\text{rot}} \gtrsim 10 \text{ km s}^{-1}$. We do not detect any broadening for any component in the studied systems, implying that all measured rotational velocities are below the 10 km s^{-1} detection threshold.

3.2.4. GP Regression

A GP is used to model noise, both instrumental and astrophysical; it is defined as a collection of random variables for which any finite number have a Gaussian distribution with a specified covariance structure. When using GPs, we use the data to condition the GP prior so that the GPs are normally distributed with respect to the data. A significant advantage of GP modeling is that it handles correlations in the data that are poorly understood by specifying only the high-level properties of a covariance kernel. We elected to use GPs to address the issues associated with stellar variations due to spots, correlated noise, and instrumental systematics that are present in the light curves for both objects. We further incorporated a white-noise kernel to assess our computed uncertainties.

Prior to the application of GPs, we create a combined binary starlight and RV curve model using PHOEBE and EMCEE. We then apply GPs to the light-curve model, which removes the need to associate the systematics in the light curve with an explicit functional form. That way, we are able to model a wide range of systematics with a small number of tunable parameters.

The kernel, or covariance function, describes the similarity between two adjacent data points. For our kernel, we elected to use a term that approximates a Matern 3/2 function, which has

a slowly varying component and a rapidly varying one:

$$k(\tau) = \sigma^2 [(1 + 1/\epsilon)e^{-(1-\epsilon)\sqrt{3}\tau/\rho} + (1 - 1/\epsilon)e^{-(1+\epsilon)\sqrt{3}\tau/\rho}]. \quad (2)$$

The parameter ϵ controls the quality of the approximation since, in the limit as $\epsilon \rightarrow 0$, this becomes the Matern 3/2 function. For our computations, we set ϵ to 0.01. The Matern 3/2 function was selected because it is capable of modeling the noise, stellar variations, and instrumental systematics in the light curve using only two parameters, σ and ρ .

We additionally incorporated a white-noise term into our model. The purpose of this term is to ensure that our uncertainties are well estimated. Poorly estimated uncertainties lead to higher values for the jitter term (high in relation to the associated noise level) and the addition of white noise of the form

$$k(\tau_{n,m}) = \sigma^2 \delta_{n,m}, \quad (3)$$

where σ is a tunable parameter.

4. Masses and Radii for Two Example *Kepler* EBs

Here we describe the results for KIC 2445134 and KIC 3003991 to demonstrate the pipeline introduced in Section 3. These objects were selected because they are total eclipsers, have small q , and the data are adequate for us to derive precise masses and radii. We also include the effective temperatures and metallicities as derived from the SDSS DR14 (Abolfathi et al. 2018) ASPCAP (García Pérez et al. 2016) pipeline. Although ASPCAP is optimized for giant and subgiant spectra, independent tests (Wilson et al. 2018; Andrews et al. 2019) have shown that offsets between ASPCAP temperatures and metallicities for FGK dwarfs are typically well within the ASPCAP uncertainties for our targets. Binary spectra if treated as single-component can result in significant systematic bias in ASPCAP parameters (El-Badry et al. 2018), but the effects are minimal below mass ratios of $q \sim 0.4$, where our two systems lie.

4.1. KIC 2445134

KIC 2445134 comprises an F-type dwarf primary and an M-type secondary orbiting with a period of 8.4 days, and has a flux ratio of ~ 0.01 in the *Kepler* bandpass. It has a *Kepler* magnitude of 13.55 and an *H*-band magnitude of 12.40. The ASPCAP T_{eff} is $6260 \pm 170 \text{ K}$ and the metallicity is $[M/H] = -0.046 \pm 0.105$. We obtained six observations of KIC 2445134 with the HRS, which we solved as an SB1 using a mid-F-type HRS template, and three observations with APOGEE, which we solved as an SB2 using the BT-Settl templates. These measurements constrained the spectroscopic orbital parameters and allowed us to re-examine our HRS cross-correlation functions and detect the faint companion in two epochs using an HRS template for a mid M star and with correlation power slightly above the noise. Table 2 lists the date and corresponding barycentric Julian Date for each of our observations, the RVs we measure, and the associated spectrograph. Figure 1 shows the BT-Settl models corresponding to the primary and secondary components, along with the flux ratio for a synthetic EB constructed from these models. We carried out the MCMC analyses described in Section 3.2.3 on the RVs in Table 2 and the *Kepler* photometry, and derived

Table 2
HRS and APOGEE RV Measurements of KIC 2445134

UT Date	BJD - 2,400,000	V_A (km s^{-1})	V_B (km s^{-1})	Instrument
2011 Aug 27	55800.804144	9.614 ± 0.0450	...	HRS
2011 Sep 6	55810.756457	48.652 ± 0.056	-45.01 ± 3.24	HRS
2011 Sep 11	55815.724269	-15.022 ± 0.053	...	HRS
2011 Sep 24	55828.729442	57.916 ± 0.058	-68.20 ± 3.66	HRS
2011 Oct 21	55855.631824	28.320 ± 0.050	...	HRS
2011 Oct 29	55863.602364	39.702 ± 0.056	...	HRS
2011 Sep 7	55811.613072	58.55 ± 0.290	-67.79 ± 1.37	APOGEE
2011 Oct 6	55840.593338	-12.33 ± 0.22	101.92 ± 0.89	APOGEE
2011 Oct 17	55851.578523	17.48 ± 0.200	28.34 ± 0.81	APOGEE

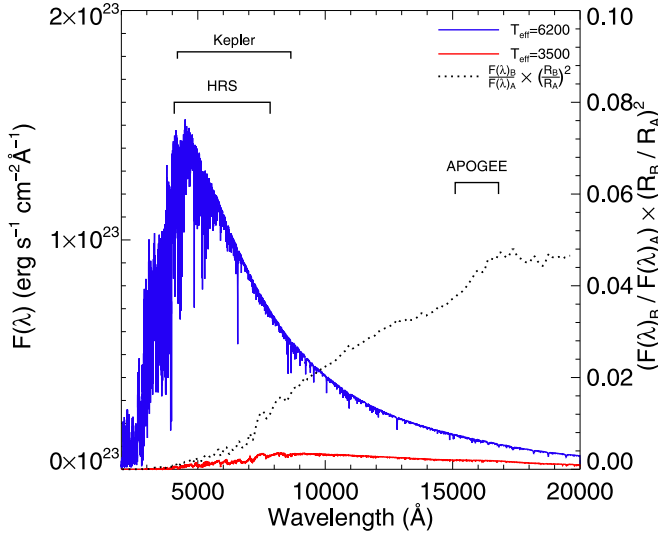


Figure 1. BT-Settl models corresponding to the components in KIC 2445134 (solid blue and red lines), and the flux ratio (dashed line). The *Kepler*, HRS, and APOGEE bandpasses are indicated for reference. The model spectra have been degraded to a spectral resolution of $R = 2000$, while the flux ratio is shown for $R = 100$. The contrast is an order of magnitude more favorable for detecting the secondary in the H -band than in the optical.

the orbital and physical parameters listed in Table 3. Figures 2 and 3 depict the models for the light curves and RV curves, respectively. Due to the large mass ratio, the temperature ratio, and the orientation of the orbit, the light curve of KIC 2445134 contains Doppler boosting. We incorporated Doppler boosting into our model using the framework of Bloemen et al. (2011) and present the Doppler boosting parameters for the primary and secondary components, B_A and B_B , respectively, in Table 3. Our measurement of the mass ratio, $q = 0.411 \pm 0.001$, has a precision of better than 1%. Our derived masses ($M_A = 1.29 \pm 0.03 M_\odot$, $M_B = 0.53 \pm 0.01 M_\odot$) and radii ($R_A = 1.42 \pm 0.01 R_\odot$, $R_B = 0.510 \pm 0.004 R_\odot$) have measurement precisions of 1% or better, except for the primary mass, which is constrained to 2%.

To assess the dependence of the parameter uncertainties on our light-curve per-point uncertainties, we ran our software in the same manner as outlined above, but with the uncertainties multiplied by 0.5 and 2 for KIC 2445134. The outcome was that all fundamental parameters remained within the 1σ uncertainties quoted, and the uncertainties were unchanged with the exception of the secondary radius uncertainty, which changed from $0.004 R_\odot$ to $0.005 R_\odot$ (still providing a 1%

Table 3
KIC 2445134 Orbital and Physical Parameters

Parameter	Value
<i>Derived Orbital Parameters</i>	
P (days)	8.41201 ± 0.00077
T_{transit}	2454972.647749
i (deg)	88.032 ± 0.001
e	0.00555 ± 0.00001
ω (rad)	4.799 ± 0.001
Ω_A	15.433 ± 0.002
Ω_B	18.4 ± 0.1
$I3$ (%)	4.0 ± 0.1
T_{peri}	2455826.85 ± 0.25
K_A (km s^{-1})	37.2 ± 0.3
K_B (km s^{-1})	90 ± 1
γ (km s^{-1})	21.6 ± 0.3
q	0.411 ± 0.001
sma (R_\odot)	21.3 ± 0.2
B_A	3.873 ± 0.002
B_B	6.098 ± 0.006
<i>Physical Parameters</i>	
M_A (M_\odot)	1.29 ± 0.03
M_B (M_\odot)	0.53 ± 0.01
R_A (R_\odot)	1.42 ± 0.01
R_B (R_\odot)	0.510 ± 0.004
T_B/T_A	0.635 ± 0.001
$T_{\text{eff } B}$ (K)	3976 ± 170
<i>Gaussian Process Parameters</i>	
$\log(\phi_{\text{Matern}})$	-0.91 ± 0.05
$\log(\rho_{\text{Matern}})$	5.09 ± 0.07
$\log(\phi_{\text{jitter}})$	-9.992 ± 0.004

uncertainty) for the case of the increased per-point uncertainties.

4.2. KIC 3003991

KIC 3003991 represents the faint end of our EB sample, with *Kepler* mag = 13.9, and comprises a late G star and a mid M star in a 7.2 day orbit with a *Kepler* flux ratio of ~ 0.005 . The ASPCAP T_{eff} is 5340 ± 140 K and the metallicity is $[M/H] = -0.41 \pm 0.073$. We obtained six observations with HRS and six observations with APOGEE. Once again, we were able to easily detect the low-mass companion in the H -band spectra, with $\alpha \sim 0.10$, and used the measurement of K_B from the APOGEE spectra to reanalyze the HRS spectra and recover the companion RV for many of the HRS epochs. The relative faintness of this EB resulted in a poorer S/N than for KIC

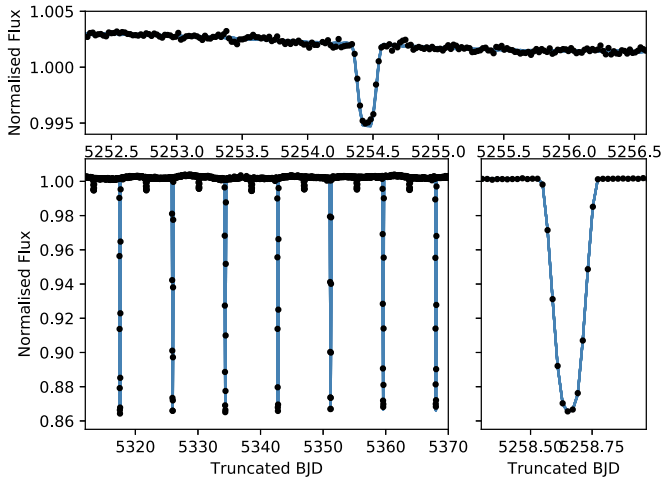


Figure 2. *Kepler* light curve (black) and ten models including GPs (blue) for KIC 2445134, where the different panels emphasize different regions of the light curve.

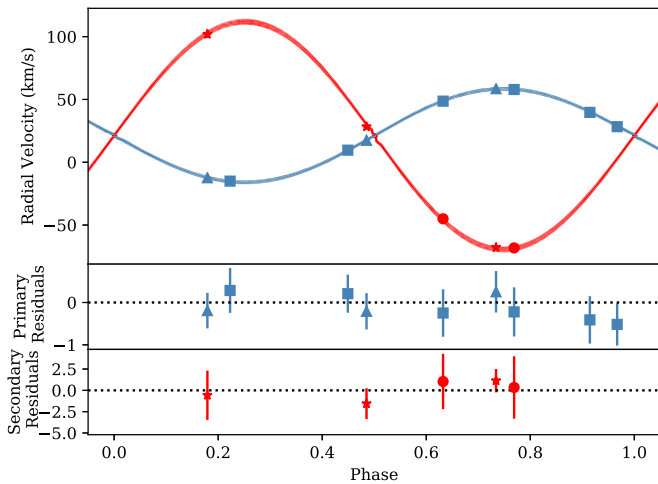


Figure 3. Phase-folded RVs for KIC 2445134 derived from the HET spectra (squares and circles) and the APOGEE spectra (triangles and stars) for the primary and secondary components, respectively. The upper panel depicts the radial velocities and ten models from the final iteration (where each model is depicted by a red or blue line). The middle and lower panels depict the residuals from the average model fit to the primary and secondary radial velocity data, respectively. The residuals are measured in km s^{-1} .

2445134 for both the APOGEE and HRS spectroscopy, which manifests as larger uncertainties on primary and secondary RVs. Table 4 lists the date and corresponding barycentric Julian Date for each of our observations, the RVs we measure, and the associated spectrograph. Figures 4 and 5 depict the light-curve model and phase-folded spectroscopic orbit for KIC 3003991, corresponding to the orbital and physical parameters in Table 5. Figure 6 shows the posterior distributions and Figure 7 shows distributions of quantities calculated from our model posteriors (where the calculations were performed after each iteration). We measure a mass ratio of $q = 0.289 \pm 0.006$, and derive masses of $M_A = 0.74 \pm 0.04 M_\odot$ and $M_B = 0.222 \pm 0.007 M_\odot$, corresponding to precisions of 5% and 3%, respectively. The uncertainty on both is driven largely by the uncertainty on the semi-amplitude, which is difficult to reduce further without a significant additional spectroscopic investment. As the precision we derive for M_B complies with our program objective of

3%, it will provide useful constraints on stellar models due to the paucity of precisely measured masses in the $M \lesssim 0.25 M_\odot$ regime. Additionally, the radii we measure for this EB, $R_A = 0.84 \pm 0.01 R_\odot$ and $R_B = 0.250 \pm 0.004 R_\odot$, have precisions of 1% and 2%, respectively.

5. False Positives in our Sample

We selected our EB sample (Table 1) in 2011, while the analysis pipeline being used by the *Kepler* team to identify EBs and substellar companions was still being refined. In a few cases, the eclipse signal detected in *Kepler* photometry results from a background EB that is spatially unresolved from the primary KIC target at the *Kepler* plate scale (Abdul-Masih et al. 2016). Many of these “false positives” have subsequently been identified by the *Kepler* team using advanced light-curve analysis of the photometry at the pixel level, and have been flagged in the *Kepler EB Catalog*. We included 14 stars now labeled as false positives for which we have APOGEE or HRS spectra to look for RV variability. In all cases, these targets show no variability within the RV measurement precisions listed in Section 2. These targets, which we have dynamically verified as false positives, are identified in the last column of Table 1. Figure 8 illustrates the attained RV precision of a star (top panel) that does not have a stellar component with a period within our baseline, amounting to better than $\sim 100 \text{ m s}^{-1}$. The magnitude and RV precision of this star are representative of stars observed from this program with the HET. The RV measurement precision of a false positive observed with APOGEE is also shown (bottom panel), and is representative of the typical RV uncertainty for our APOGEE targets.

6. Discussion and Future Prospects

The two EBs presented in Section 4 illustrate the contributions made by our ongoing work to the direct and precise measurement of masses and radii for low-mass stars. Many systems in our EB sample have primary components with mass $M > 0.8 M_\odot$, a regime where models of stellar mass and radii are well matched to observational constraints. Many have small mass ratios ($q < 0.6$), and so have low-mass secondaries, specifically targeting the regime with disagreement between models and existing observations. The high-mass primary allows traditional spectroscopic analysis tools to obtain metallicity for the spectra since the secondary star flux is low enough that the effect of spectral contamination is minimal. As discussed in Terrien et al. (2012) the stellar metallicity is an important constraint on the models, as well as being necessary to derive ages. This project aims to derive masses and radii for low-mass stars using a combination of precision photometry from *Kepler* coupled with radial velocities from stable fiber-fed optical and near-infrared high-resolution spectrographs. Figure 9 depicts the mass–radius relationship for the stars in this work (filled blue and black circles), compared with those from DEBCat (open circles). Figure 10 depicts the same but with $[\text{Fe}/\text{H}] = -1$ isochrones (as opposed to solar metallicity). The primary and secondary components of KIC 2445134 both show good agreement (within 1σ) with the 2 Gyr solar metallicity isochrones. The primary component of KIC 3003991 shows good agreement (within 1σ) with the 10 Gyr isochrones, but the secondary component is 3σ away. This kind of disagreement is not unusual in the literature for low-mass stars (Torres et al. 2010). Our program with

Table 4
HRS and APOGEE RV Measurements of KIC 3003991

UT Date	BJD - 2,400,000	V_A (km s^{-1})	V_B (km s^{-1})	Instrument
2011 Oct 8	55842.687885	-144.119 ± 0.072	-50.68 ± 8.35	HRS
2012 Mar 21	56007.990683	-120.157 ± 0.065	...	HRS
2012 Apr 24	56041.897439	-101.114 ± 0.064	-201.51 ± 7.01	HRS
2012 May 28	56075.798304	-143.297 ± 0.061	-50.92 ± 8.21	HRS
2012 Jun 8	56086.797501	-103.329 ± 0.064	-185.18 ± 12.08	HRS
2012 Jun 10	56088.766870	-140.972 ± 0.06	-54.93 ± 5.63	HRS
2011 Sep 9	55813.6973400	-144.110 ± 0.290	-39.99 ± 4.58	APOGEE
2011 Sep 19	55823.7244600	-115.150 ± 0.200	-151.93 ± 4.65	APOGEE
2011 Oct 6	55840.6597900	-106.210 ± 0.310	-165.85 ± 6.30	APOGEE
2011 Oct 15	55849.5774200	-139.530 ± 0.200	-69.54 ± 3.22	APOGEE
2011 Oct 17	55851.6479100	-136.690 ± 0.170	-72.76 ± 3.51	APOGEE
2011 Nov 1	55866.5693400	-128.360 ± 0.170	-96.77 ± 4.51	APOGEE

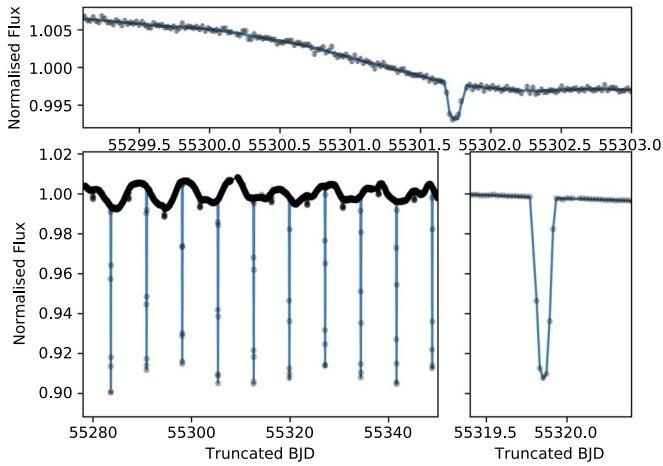


Figure 4. *Kepler* light curve (black) and ten models including GPs (blue) for KIC 3003991, where the different panels emphasize different regions of the light curve.

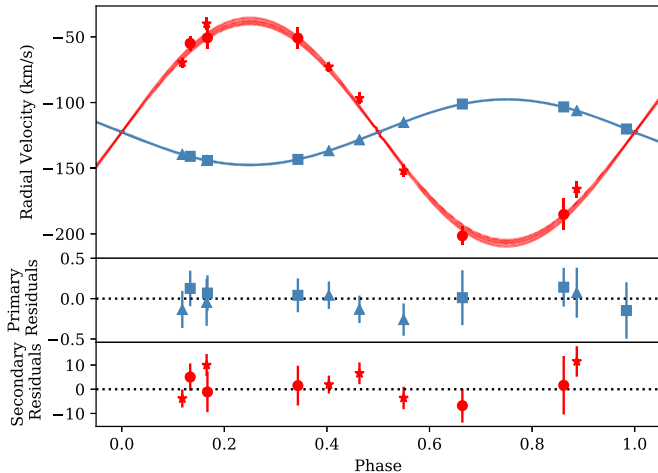


Figure 5. Phase-folded RVs for KIC 3003991. The layout is identical to Figure 3. The thickness of the lines depicts the spread of the ten models caused by the model uncertainty. This is particularly significant for the secondary component (red lines).

APOGEE will continue to fill in parameter space by obtaining double-line spectroscopic RVs for systems with high flux contrast. KIC 2445134 and KIC 3003991 would have been especially challenging without the benefit of NIR spectroscopy.

Table 5
KIC 3003991 Orbital and Physical Parameters

Parameter	Value
<i>Derived Orbital Parameters</i>	
P (days)	7.24478 ± 0.00062
T_{transit}	2454964.859085
i (deg)	88.178 ± 0.008
e	0.00030 ± 0.00003
ω (rad)	4.09 ± 0.03
Ω_A	18.76 ± 0.02
Ω_B	19.9 ± 0.3
$I3$ (%)	3.5 ± 0.2
$T_{\text{peri.}}$	2455953.65 ± 0.18
K_A (km s^{-1})	24.97 ± 0.05
K_B (km s^{-1})	83 ± 1
γ (km s^{-1})	-122.55 ± 0.03
q	0.298 ± 0.006
sma (R_{\odot})	15.6 ± 0.2
<i>Physical Parameters</i>	
M_A (M_{\odot})	0.74 ± 0.04
M_B (M_{\odot})	0.222 ± 0.007
R_A (R_{\odot})	0.84 ± 0.01
R_B (R_{\odot})	0.250 ± 0.004
T_B/T_A	0.662 ± 0.001
$T_{\text{eff } B}$ (K)	3536 ± 140
<i>Gaussian Process Parameters</i>	
$\log(\phi_{\text{Matern}})$	-0.3 ± 0.1
$\log(\rho_{\text{Matern}})$	4.3 ± 0.1
$\log(\phi_{\text{jitter}})$	-10.996 ± 0.004

For these systems we succeeded in obtaining the 3% program goal for the uncertainties on the masses and radii (with the exception of the primary mass of KIC 3003991), making these valuable benchmark systems. Additional results emerging from this program will further populate the mass–radius plane for low-mass dwarfs, study systems with equal-mass components, and provide high-precision checks on parameters derived from asteroseismology for a few, rare giants in EB systems with detected stellar oscillations.

We acknowledge support from two NASA ADAP grants (NNX13AF32G and 16-ADAP16-0201), and NSF grant AST 1517592 for this project. This work was partially supported by funding from the Center for Exoplanets and Habitable Worlds. The Center for Exoplanets and Habitable Worlds is supported

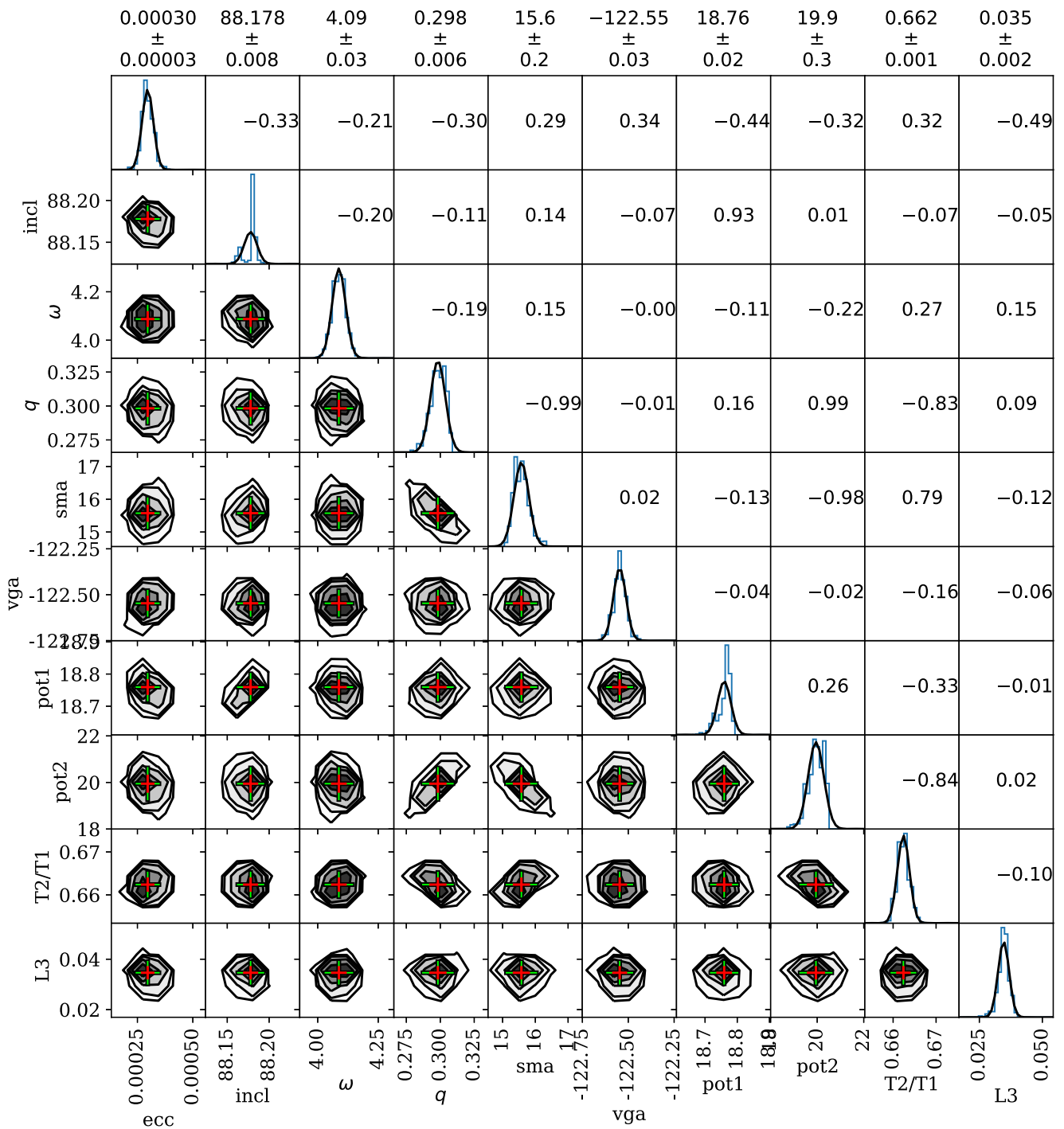


Figure 6. Posterior distributions for the KIC 3003991 parameters derived from *Kepler* photometry, and APOGEE and HRS radial velocities. Boxes in the upper right contain the standard correlation coefficient, with 1 corresponding to perfect correlation, -1 perfect anticorrelation, and 0 no correlation. Final parameter values are listed along the top.

by the Pennsylvania State University, the Eberly College of Science, and the Pennsylvania Space Grant Consortium. We acknowledge support from NSF grants AST 1006676 and AST 1126413 in our pursuit of precision radial velocities in the NIR. This research has made use of the SIMBAD database, operated at CDS, Strasbourg, France. This publication makes use of data products from the Two Micron All Sky Survey, which is a joint project of the University of Massachusetts and the Infrared Processing and Analysis Center/California Institute of Technology, funded by the National Aeronautics and Space

Administration and the National Science Foundation. Finally, we acknowledge the thorough review of the anonymous reviewer whose comments saved us from a small embarrassment.

This work was based on observations with the SDSS 2.5 m telescope. Funding for SDSS-III has been provided by the Alfred P. Sloan Foundation, the Participating Institutions, the National Science Foundation, and the U.S. Department of Energy of Science. The SDSS-III website is <http://www.sdss3.org/>. SDSS-III is managed by the Astrophysical Research

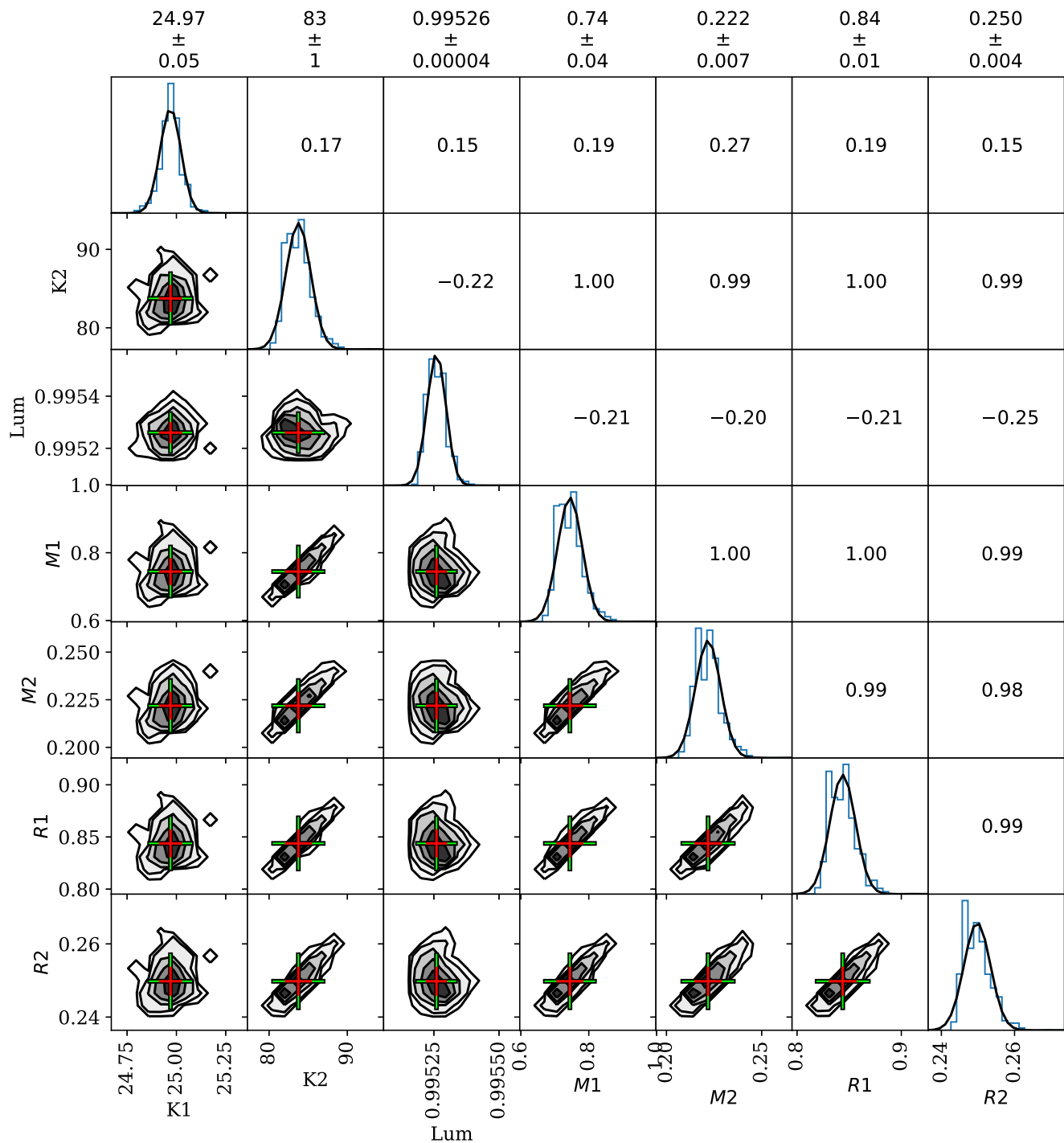


Figure 7. Parameter distributions for the calculated parameters of KIC 3003991. Layout is as in Figure 6.

Consortium for the Participating Institutions of the SDSS-III Collaboration including the University of Arizona, the Brazilian Participation Group, Brookhaven National Laboratory, University of Cambridge, Carnegie Mellon University, University of Florida, the French Participation Group, the German Participation Group, Harvard University, the Instituto de Astrofísica de Canarias, the Michigan State/Notre Dame/JINA Participation Group, Johns Hopkins University, Lawrence Berkeley National Laboratory, Max Planck Institute for Astrophysics, Max Planck Institute for Extraterrestrial Physics, New Mexico State University, New York University, Ohio State University, Pennsylvania State University, University of

Portsmouth, Princeton University, the Spanish Participation Group, University of Tokyo, University of Utah, Vanderbilt University, University of Virginia, University of Washington, and Yale University.

Data presented herein were also obtained at the Hobby–Eberly Telescope (HET), a joint project of the University of Texas at Austin, the Pennsylvania State University, Stanford University, Ludwig-Maximilians-Universität München, and Georg-August-Universität Göttingen. The HET is named in honor of its principal benefactors, William P. Hobby and Robert E. Eberly.

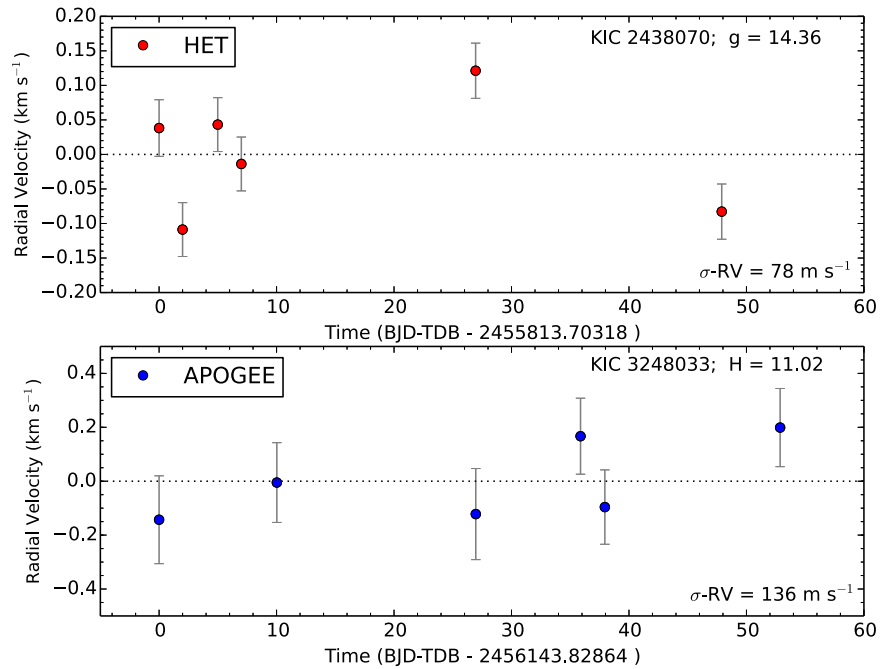


Figure 8. RV measurements of KIC 3248033 identified as a false positive based on pixel-level analysis of its photometry and of the red giant KIC 2438070 with no stellar eclipsing companion. Our RV measurements dynamically verify that the eclipse signal in the light-curve data results from an unresolved background EB which is highly diluted by the foreground KIC target.

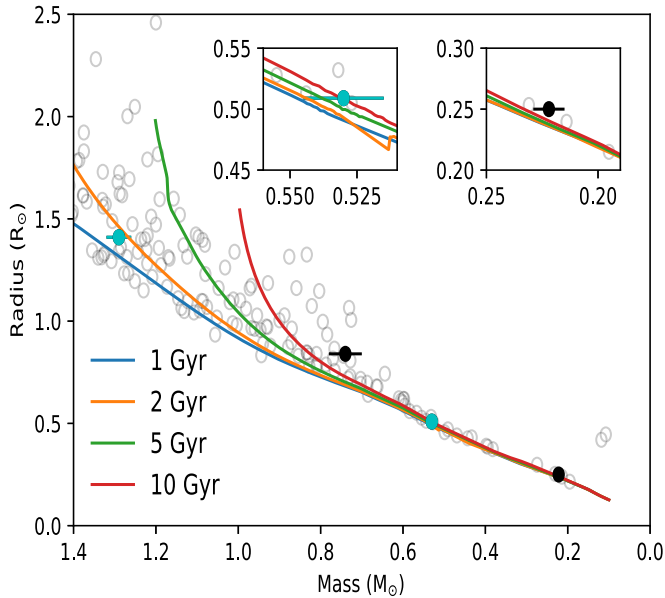


Figure 9. Radius vs. mass, plotted for the EBs in the DEBCat Eclipsing Binary Catalog (open circles), along with the two EBs we describe in Section 4, where KIC 2445134 is depicted with solid blue circles and KIC 3003991 is depicted with solid black circles. For comparison, we show MIST (MESA Isochrones and Stellar Tracks) stellar isochrones (Choi et al. 2016; Dotter 2016) for stars of solar metallicity. The insets depict magnified regions for the secondary components of KIC 2445134 (left) and KIC 3003991 (right). The paucity of precision measurements below $\sim 0.8 M_{\odot}$, and particularly below $\sim 0.25 M_{\odot}$, is evident.

Appendix

Detailed Description of Our HET HRS Pipeline

Our EB project makes use of an internal data reduction pipeline for the HRS on HET. For future reference with other papers in this series, and for others using this instrument on the HET, we provide a detailed description of our pipeline, which

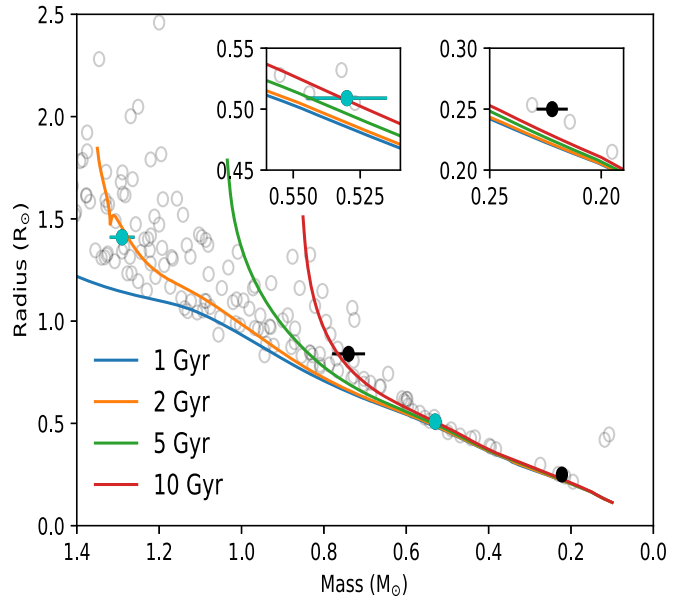


Figure 10. The same as Figure 9, but with $[\text{Fe}/\text{H}] = -1$. In this case, the primary component of KIC 3003991 now agrees with the 10 Gyr isochrone, but the secondary component does not. This is in line with a known disparity between theoretical stellar models and observations in the low-mass region, and further highlights the importance of modeling low-mass binary components (Torres et al. 2010).

is composed of a series of independent subroutines that can be combined into nightly processing scripts; we refer to on-sky observations of science targets generically as target frames, and individual calibrations either generically as calibrations or by their specific function. As an aside, the pipeline can easily process HRS data taken in any of the possible HRS configurations, and so, as a service to other observers who may be interested in utilizing its functionality, the description

we provide here is intended to be general, rather than specific to the HRS configuration listed above.

A raw HRS FITS image contains three components: the main FITS header describes the instrument configuration and target exposure, while the first and second FITS extensions contain the red and blue image data, respectively. Instrument keywords in the main header can reliably reconstruct the HRS configuration used for any given observation, without relying on external log sheets or records. Keywords describing the target, such as `OBSTYPE` and `OBJECT`, are manually specified by the HET resident astronomer carrying out the observation, and are not always used consistently. To begin reducing a night's observations, we copy the raw target and calibration images into a single working directory. The pipeline automatically classifies the various calibration and target frames, and carries out basic image processing on them. If the working directory contains images taken with different HRS configurations, each configuration will be parsed and handled automatically.

First, `HRS_SPLIT` extracts the red and blue images from the multi-extension FITS file, saves them as individual zero-extension FITS images with a suffix of “_r” or “_b,” and assigns the data contained in the original header. This step ensures that the original FITS files are not modified in any way by the pipeline. We then perform an overscan correction (`HRS_OVERSCAN`) by trimming each image to the data region and subtracting a pedestal value determined by computing the median of the overscan region. Higher order corrections that could be derived from the overscan are instead corrected with the bias frames. Different HRS configurations utilize different on-chip CCD binning schemes, and `HRS_BIAS` automatically groups and combines bias frames based on their binning, producing master bias frames for each configuration used during a night. A similar process is then performed on all available flat fields (`HRS_FLAT`), although the number of possible configurations is much larger for flats than for bias frames. `HRS_FLAT` properly separates multiple sets of flats from the same configuration that were obtained with different exposure times, which is occasionally necessary when flats with very high signal-to-noise ratio are required. In addition, non-standard flat fields taken through the HRS target fibers illuminated by the Medium Resolution Spectrograph (Ramsey et al. 2003) flat lamp or twilight sky are properly recognized. Each master flat field is automatically bias-corrected and saved with a unique name identifying the light source, instrument configuration, and exposure time. Similar corrections are applied to individual target frames. These image processing steps can generally be carried out without any human input or supervision, and are conveniently grouped in a script, `HRS_IPROC`, which requires no input parameters or keywords.

Extracting one-dimensional spectra from a two-dimensional image requires locating and tracing each echelle order in the target image. The HRS dispersion runs vertically across the detector (our y coordinate), and we make the simplifying (but essentially correct) assumption that the HRS slit is aligned perfectly with detector pixel rows (our x coordinate). Each order is traced independently, and each trace begins by identifying one x and y pair that intercepts the fiber profile. At that position we extract a subarray with an x dimension of 1.5 times the physical width of the fiber in pixels, which fully encloses the illuminated pixels without overlapping into the adjacent orders, and a y dimension of 4 pixels, which averages

over noise and increases the speed of the tracing procedure. The illumination profile of a fiber resembles a top hat, with some variation across the illuminated pixels due to imperfect radial scrambling in the fiber. This functional form is not well represented by the Gaussian profile commonly used for slit-fed spectrographs. Instead, to identify the x coordinate of the beam center we compute the derivative of the profile and fit that with a combination of two Gaussians of equal width, separated by the slit width in pixels. This parameterization reliably recovers the beam center position at the selected y coordinate. The algorithm then walks up and down the beam, computing x for each binned y . We fit these measured beam positions with a low-order polynomial to derive the beam position at each dispersion position.

The tracing algorithm is implemented in two separate subroutines: `HRS_MTRACE` and `HRS_ATRACE`. `HRS_MTRACE` allows the user to interactively identify beams, and annotate each with the echelle order and the type of spectrum (absorption, such as a target or flat field, or emission, such as a sky or ThAr). This information is encapsulated in a template file that fully describes the HRS configuration. `HRS_ATRACE` is fully automated, and uses previously derived templates to process routine sets of images, retracing all beams to compensate for any misalignment between the template and the target frame due to imprecision in repositioning the HRS components.

Preserving the relative flux information in our science target frames requires that the master flat frames be normalized to remove both the echelle blaze and the fiber illumination profile. `HRS_FLATNORM` derives this normalization, using a procedure conceptually similar to optimal spectral extraction. Such schemes have been described extensively in the past (e.g., Horne 1986; Mukai 1990; Cushing et al. 2004), and we have adapted them for use with a fiber-fed echelle spectrograph. Each master flat is traced, and then each beam is rectified. The rectified beam is used to derive a dispersion-dependent spatial profile for the beam, following the procedure outlined by Cushing et al. (2004) and figures therein. This profile is the desired function for normalizing the flat fields. Reversing the image rectification on the beam profile yields the normalization image that can be applied to the original master flat frame.

To extract the individual target spectra, `HRS_OPTEXT` divides the normalized flat field into the two-dimensional target image, and then applies an optimal extraction algorithm similar to that used for normalizing the flat fields. If multiple exposures of the same target were obtained, the user has the option to extract each image individually, or coadd them in two dimensions and extract the composite spectrum. Optimal fiber profiles are automatically derived for each beam, and provide the proper weighting functions for optimal extraction. A primary benefit often associated with optimal extraction algorithms is their ability to optimize the S/N of the extracted spectrum by minimizing the contribution of detector noise. While this is useful for some of our fainter *Kepler* EB targets, more useful is the algorithm's ability to automatically identify bad pixels in the two-dimensional images caused by detector defects or cosmic rays. These pixels are automatically excluded and the weighting function at each affected dispersion element is adjusted accordingly. `HRS_OPTEXT` returns optimally extracted spectra, sum-extracted spectra for comparison purposes, and wavelength-dependent variances that provide realistic measures of the spectrum S/N. These data products, as

well as descriptions of each echelle order and beam, are encapsulated in a FITS table for each target image.

Our wavelength calibration pipeline relies on a construct similar to that behind the tracing algorithms: time-intensive manual line identification defines templates for each HRS configuration, and these templates are used in an automated re-identification procedure for routine data processing. The templates are generated using the IDL-based WAVECAL package (Piskunov & Valenti 2002) to associate the wavelengths of known ThAr spectral lines with their y pixel location for each spectral order. Wavelengths are taken from the linelist of Murphy et al. (2007), and typically number ~ 10 – 20 per order. The set of lines comprising each order is fit with a low-order polynomial (typically fourth order) to derive the template dispersion solution for that order. To calibrate a target spectrum, we automatically measure the ThAr image taken consecutively to the target observation, using the template as a guide. The dispersion solution for each order is automatically solved for, using a sigma-clipping rejection to detect poorly fit lines, and the resulting wavelength solution is applied to the corresponding target spectrum. Although the HRS is not a pressure- or temperature-stabilized instrument, this careful use of ThAr calibrations consecutive with target observations can yield RV stability of 25 m s^{-1} or better for observations taken on different nights, weeks, or even months (e.g., Bender et al. 2012).

ORCID iDs

Suvrath Mahadevan  <https://orcid.org/0000-0001-9596-7983>

Chad F. Bender  <https://orcid.org/0000-0003-4384-7220>

Kelly Hambleton  <https://orcid.org/0000-0001-5473-856X>

Scott W. Fleming  <https://orcid.org/0000-0003-0556-027X>

Kyle Conroy  <https://orcid.org/0000-0002-5442-8550>

Leslie Hebb  <https://orcid.org/0000-0003-1263-8637>

Arpita Roy  <https://orcid.org/0000-0001-8127-5775>

Andrej Prša  <https://orcid.org/0000-0002-1913-0281>

References

- Abdul-Masih, M., Prša, A., Conroy, K., et al. 2016, *AJ*, **151**, 101
- Abolfathi, B., Aguado, D. S., Aguilar, G., et al. 2018, *ApJS*, **235**, 42
- Ahn, C. P., Alexandroff, R., Allende Prieto, C., et al. 2013, arXiv:1307.7735
- Allard, F., Homeier, D., & Freytag, B. 2011, ASP Conf. Ser. 448 in 16th Cambridge Workshop on Cool Stars, Stellar Systems, and the Sun (San Francisco, CA: ASP), 91
- Allende Prieto, C., Majewski, S. R., Schiavon, R., et al. 2008, *AN*, **329**, 1018
- Andersen, J. 1991, *A&ARv*, **3**, 91
- Andrews, J. J., Anguiano, B., Chanamé, J., et al. 2019, *ApJ*, **871**, 42
- Bender, C. F., Mahadevan, S., Deshpande, R., et al. 2012, *ApJL*, **751**, L31
- Bender, C. F., & Simon, M. 2008, *ApJ*, **689**, 416
- Berger, D. H., Gies, D. R., McAlister, H. A., et al. 2006, *ApJ*, **644**, 475
- Bloemen, S., Marsh, T. R., Østensen, R. H., et al. 2011, *MNRAS*, **410**, 1787
- Borucki, W. J., Koch, D., Basri, G., et al. 2010, *Sci*, **327**, 977
- Caldwell, D. A., Kolodziejczak, J. J., Van Cleve, J. E., et al. 2010, *ApJL*, **713**, L92
- Carter, J. A., Fabrycky, D. C., Ragozzine, D., et al. 2011, *Sci*, **331**, 562
- Casewell, S. L., Raynard, L., Watson, C. A., et al. 2018, *MNRAS*, **481**, 1897
- Castelli, F., & Kurucz, R. L. 2004, arXiv:astro-ph/0405087
- Chabrier, G., Gallardo, J., & Baraffe, I. 2007, *A&A*, **472**, L17
- Choi, J., Dotter, A., Conroy, C., et al. 2016, *ApJ*, **823**, 102
- Claret, A., Hauschildt, P. H., & Witte, S. 2012, *A&A*, **546**, A14
- Conroy, K. E., Prša, A., Stassun, K. G., et al. 2014, *PASP*, **126**, 914
- Cruz, P., Diaz, M., Birkby, J., et al. 2018, *MNRAS*, **476**, 5253
- Cushing, M. C., Vacca, W. D., & Rayner, J. T. 2004, *PASP*, **116**, 362
- Diaz-Cordoves, J., & Gimenez, A. 1992, *A&A*, **259**, 227
- Dittmann, J. A., Irwin, J. M., Charbonneau, D., et al. 2017, *ApJ*, **836**, 124
- Dotter, A. 2016, *ApJS*, **222**, 8
- Doyle, L. R., Carter, J. A., Fabrycky, D. C., et al. 2011, *Sci*, **333**, 1602
- Eisenstein, D. J., Weinberg, D. H., Agol, E., et al. 2011, *AJ*, **142**, 72
- El-Badry, K., Rix, H.-W., Ting, Y.-S., et al. 2018, *MNRAS*, **473**, 5043
- Faigler, S., & Mazeh, T. 2011, *MNRAS*, **415**, 3921
- Faigler, S., Mazeh, T., Quinn, S. N., Latham, D. W., & Tal-Or, L. 2012, *ApJ*, **746**, 185
- Feiden, G. A., & Chaboyer, B. 2013, *ApJ*, **779**, 183
- Feiden, G. A., Chaboyer, B., & Dotter, A. 2011, *ApJL*, **740**, L25
- Foreman-Mackey, D., Agol, E., Ambikasaran, S., & Angus, R. 2017, celerite, Astrophysics Source Code Library, ascl:1709.008
- Foreman-Mackey, D., Hogg, D. W., Lang, D., & Goodman, J. 2013, *PASP*, **125**, 306
- García Pérez, A. E., Allende Prieto, C., Holtzman, J. A., et al. 2016, *AJ*, **151**, 144
- Gómez Maqueo Chew, Y., Morales, J. C., Faedi, F., et al. 2014, *A&A*, **572**, A50
- Goodman, J., & Weare, J. 2010, *Communications in Applied Mathematics and Computational Science*, **5**, 65
- Goodricke, J. 1783, *Royal Society of London Philosophical Transactions Series I*, **73**, 474
- Gray, D. F. 1992, *The Observation and Analysis of Stellar Photospheres* (Cambridge: Cambridge Univ. Press)
- Gunn, J. E., Siegmund, W. A., Mannery, E. J., et al. 2006, *AJ*, **131**, 2332
- Higl, J., & Weiss, A. 2017, *A&A*, **608**, A62
- Home, K. 1986, *PASP*, **98**, 609
- Husser, T.-O., Wende-von Berg, S., Dreizler, S., et al. 2013, *A&A*, **553**, A6
- Irwin, J. M., Quinn, S. N., Berta, Z. K., et al. 2011, *ApJ*, **742**, 123
- Kesseli, A. Y., Kirkpatrick, J. D., Fajardo-Acosta, S. B., et al. 2018, arXiv:1810.07702
- Kirk, B., Conroy, K., Prša, A., et al. 2016, *AJ*, **151**, 68
- Konacki, M., Muterspaugh, M. W., Kulkarni, S. R., & Helminiak, K. G. 2010, *ApJ*, **719**, 1293
- Kraus, A. L., Tucker, R. A., Thompson, M. I., Craine, E. R., & Hillenbrand, L. A. 2011, *ApJ*, **728**, 48
- Lockwood, A. C., Johnson, J. A., Bender, C. F., et al. 2014, arXiv:1402.0846
- López-Morales, M. 2007, *ApJ*, **660**, 732
- Lubin, J. B., Rodriguez, J. E., Zhou, G., et al. 2017, *ApJ*, **844**, 134
- Lucy, L. B. 1967, *ZA*, **65**, 89
- MacDonald, J., & Mullan, D. J. 2017, *ApJ*, **850**, 58
- Majewski, S. R., Schiavon, R. P., Frinchaboy, P. M., et al. 2017, *AJ*, **154**, 94
- Markwardt, C. B. 2009, adass XVIII, **411**, 251
- Matijević, G., Prša, A., Orosz, J. A., et al. 2012, *AJ*, **143**, 123
- Mazeh, T., Simon, M., Prato, L., Markus, B., & Zucker, S. 2003, *ApJ*, **599**, 1344
- Mighell, K. J., & Plavchan, P. 2013, *AJ*, **145**, 148
- Morales, J. C., Gallardo, J., Ribas, I., et al. 2010, *ApJ*, **718**, 502
- Morales, J. C., Ribas, I., & Jordi, C. 2008, *A&A*, **478**, 507
- Mukai, K. 1990, *PASP*, **102**, 183
- Murphy, M. T., Tzanavaris, P., Webb, J. K., & Lovis, C. 2007, *MNRAS*, **378**, 221
- Nidever, D. L., Holtzman, J. A., Allende Prieto, C., et al. 2015, *AJ*, **150**, 173
- Piskunov, N. E., & Valenti, J. A. 2002, *A&A*, **385**, 1095
- Planck, M. 1900a, *V. Deut. Phys. Ges.*, **2**, 202
- Planck, M. 1900b, *V. Deut. Phys. Ges.*, **2**, 237
- Popper, D. M. 1980, *ARA&A*, **18**, 115
- Prato, L., Simon, M., Mazeh, T., et al. 2002, *ApJ*, **569**, 863
- Prša, A., Batalha, N., Slawson, R. W., et al. 2011, *AJ*, **141**, 83
- Prša, A., Conroy, K. E., Horvat, M., et al. 2016, *ApJS*, **227**, 29
- Prša, A., & Harmanec, P. 2012, IAU Symp. 282 in From Interacting Binaries to Exoplanets: Essential Modeling Tools, ed. M.T. Richards & I. Hubeny (Cambridge: Cambridge Univ. Press), 339
- Prša, A., & Zwitner, T. 2005, *ApJ*, **628**, 426
- Ramsey, L. W., Adams, M. T., Barnes, T. G., et al. 1998, *Proc. SPIE*, **3352**, 34
- Ramsey, L. W., Engel, L. G., Sessions, N., et al. 2003, *Proc. SPIE*, **4841**, 1036
- Ruciński, S. M. 1969a, *AcA*, **19**, 125
- Ruciński, S. M. 1969b, *AcA*, **19**, 245
- Schwamb, M. E., Orosz, J. A., Carter, J. A., et al. 2013, *ApJ*, **768**, 127
- Shetrone, M., Cornell, M. E., Fowler, J. R., et al. 2007, *PASP*, **119**, 556
- Slawson, R. W., Prša, A., Welsh, W. F., et al. 2011, *AJ*, **142**, 160
- Tal-Or, L., Faigler, S., & Mazeh, T. 2015, *A&A*, **580**, A21
- Terrien, R. C., Fleming, S. W., Mahadevan, S., et al. 2012, *ApJL*, **760**, L9
- Terrien, R. C., Mahadevan, S., Deshpande, R., et al. 2014, *ApJ*, **782**, 61
- Tonry, J., & Davis, M. 1979, *AJ*, **84**, 1511
- Torres, G., Andersen, J., & Giménez, A. 2010, *A&ARv*, **18**, 67
- Tull, R. G. 1998, *Proc. SPIE*, **3355**, 387

- von Zeipel, H. 1924, [MNRAS](#), **84**, 702
- Wilson, J. C., Hearty, F., Skrutskie, M. F., et al. 2010, [Proc. SPIE](#), **7735**, 77351C
- Wilson, R. E. 1979, [ApJ](#), **234**, 1054
- Wilson, R. E. 1993, ASP Conf. Ser. 38 in New frontiers in binary star research, ed. K.-C. Leung & Il-Seong Nha (San Francisco, CA: ASP), 91
- Wilson, R. E. 2007, [A&AT](#), **26**, 3
- Wilson, R. E., & Devinney, E. J. 1971, [ApJ](#), **166**, 605
- Wilson, R. E., & Wyithe, S. B. 2003, ASP Conf. Ser. 298 in GAIA Spectroscopy: Science and Technology, ed. U. Munari (San Francisco, CA: ASP), 313
- Wilson, R. F., Teske, J., Majewski, S. R., et al. 2018, [AJ](#), **155**, 68
- York, D. G., Adelman, J., Anderson, J. E., Jr., et al. 2000, [AJ](#), **120**, 1579
- Zasowski, G., Johnson, J. A., Frinchaboy, P. M., et al. 2013, [AJ](#), **146**, 81
- Zhou, G., Bayliss, D., Hartman, J. D., et al. 2015, [MNRAS](#), **451**, 2263
- Zucker, S. 2003, [MNRAS](#), **342**, 1291
- Zucker, S., & Mazeh, T. 1994, [ApJ](#), **420**, 806